# Thin-Layer Full Navier-Stokes Simulations over a Supersonic Delta Wing

W. Phillip Webster* and Joseph S. Shang†
*U.S. Air Force Wright Research and Development Center, Wright-Patterson Air Force Base, Ohio 45433*

**Steady flowfields describing the flow over a 75-deg swept delta wing at $M_\infty = 1.95$ and $4.48 \times 10^6$ were simulated at $\alpha = 20$ and 30 deg using two computer codes. Comparisons were made between calculations using 1) the laminar and turbulent thin-layer Navier-Stokes equations, and 2) laminar thin-layer and Navier-Stokes equations. At $\alpha = 20$ deg, each equation set captures the essential structure of the flow and the differences between their results are minor. Numerical results generated by a grid refinement study exhibited only a minor improvement. The Navier-Stokes equations were used to calculate the flow at $\alpha = 30$ deg. A region of reversed flow along the surface near the trailing edge was observed. The vertical extent of this region was much smaller, but the upstream propagation extended much farther than the thin-layer simulation.**

## Nomenclature

| | |
|---|---|
| $C_p$ | = coefficient of pressure |
| $L$ | = root chord length |
| $M$ | = Mach number |
| $Re$ | = Reynolds number |
| $U, V, W$ | = velocity components in coordinate directions |
| $x, y, z$ | = coordinate directions |
| $Y$ | = maximum span at a given $x$ location |
| $y^+$ | = nondimensional distance from surface, $z\sqrt{\tau_0/\rho}/\nu$) |
| $\alpha$ | = angle of attack |
| $\beta$ | = leading-edge bevel |
| $\Gamma$ | = sweep angle |
| $\rho$ | = density |
| $\tau$ | = surface shear stress |
| $\infty$ | = freestream value |
| 0 | = surface value |

## Introduction

THE flow about modern high-speed aircraft with a delta planform at angle of attack is characterized by the presence of large spiraling vortices on the lee side of the wing. In many cases, these vortices are the primary structure in the flow affecting the performance of the aircraft. These vortices readily form at low angles of attack. With increasing angle of attack, secondary and tertiary vortices form due to boundary-layer separation. Flows over slender delta wings have been studied experimentally by Monnerie and Werle,[1], Hummel,[2] Miller and Wood,[3] Stallings and Lamb,[4] and Guyton,[5] among others; they have been studied numerically by Rizzetta and Shang,[6] Buter and Rizzetta,[7] Thomas and Newsome,[8] to name but a few. There have been numerous investigations of other delta-based planforms. These include, but are not limited to, delta wings with canard,[9] crank delta wings,[10] pitching delta wings,[11] and rocking delta wings.[12]

In a previous paper,[13] the authors presented numerical simulations of vortical flow over a delta wing ($\Gamma = 75$ deg) at four angles of attack (10, 20, 30, and 35 deg) at a freestream Mach number of 1.95 and a Reynolds number of $4.48 \times 10^6$. The governing equations used were the unsteady, compressible, three-dimensional, thin-layer Navier-Stokes equations written in Reynolds averaged form. The computer code used to solve this set of equations was ARC3D, which is fully described by Pulliam.[14] This code uses the approximately factorized implicit Beam-Warming algorithm and is diagonalized to accelerate convergence.

The previous results captured the essential structure of the vortical flow on the lee side of the delta wing. At $\alpha = 10$ and 20 deg, the results compared very favorably with experimental results. At $\alpha = 30$ and 35 deg, a large region of reversed flow was observed near the trailing edge. This reversed flow was contained in the low-pressure region associated with the secondary vortex. It extended from the trailing edge forward to 67% of the root chord for $\alpha = 30$ deg and forward to 56% of the root chord at $\alpha = 35$ deg.

This work left three areas in which the results were not satisfactory. The first problem area was the assumption of laminar flow. The high Reynolds number ($4.48 \times 10^6$ based on root chord length) would indicate the flow to be turbulent. However, to focus the range of issues in the previous work, turbulence was not modeled. The second issue was the use of the thin-layer assumption. The thin-layer assumption is considered appropriate for vortical flows; however, its utility is unknown in the reversed flow region where stress components in the spanwise direction may not be negligible. The final problem area was the need for a grid resolution study that was not performed in the previous work.

Addressing each of these issues is the objective of this paper. In order to do this, a second computer code was used to solve the Navier-Stokes equations. This code (FDL3D-I), written by Visbal,[15] is based, like ARC3D, on the approximately factorized implicit Beam-Warming algorithm; however, it has several differences from ARC3D. First, the code can solve either the full or thin-layer Navier-Stokes equations. Second, the code is not diagonalized but retains the block tridiagonal form; thus, it is first-order accurate in time. In addition to these major differences, there are several smaller differences between the two codes. Since FDL3D-I retains the block tridiagonal structure, the implicit damping terms are second order. Because of its scalar pentadiagonal form, ARC3D has both second- and fourth-order terms. In addition, the metric terms at boundaries in ARC3D are first-order accurate, whereas in FDL3D-I, they are second order.

In order to compare the codes as carefully as possible, the damping terms were maintained as nearly identical as possible. The coefficients for the second- and fourth-order explicit and second-order implicit were the same. To match the fourth-

Presented as Paper 90-0589 at the AIAA 28th Aerospace Sciences Meeting, Reno, NV, Jan. 8-11, 1990; received Feb. 8, 1990; revision received Sept. 27, 1990; accepted for publication Oct. 21, 1990. 

*Aerospace Engineer, WL/FIMM. Member AIAA.
†Technical Manager, WL/FIMM. Associate Fellow AIAA.

order implicit term from ARD3D, additional second-order implicit damping was added to FDL3D. This results in the codes solving slightly different sets of equations, and small differences in the results were to be expected. One method to avoid this difference would have been not to use fourth-order damping; however, the solution became unstable.

The resolution of the issues just outlined was accomplished in the following manner. First, the effects of turbulence were evaluated using ARC3D. This was done since ARC3D has an implementation of the Baldwin-Lomax turbulence model, which is currently unavailable in FDL3D-I. Second, FDL3D-I was used to calculate the flowfield about a delta wing using the thin-layer approximation to validate FDL3D-I. This calculation used the same conditions and grid as the previous work at $\alpha = 20$ deg. These results were compared to the previous results as well as to experimental data. Third, the full Navier-Stokes equations were solved using FDL3D-I and compared to the thin-layer results, such that observed variations in the results could be attributed to the use of thin-layer or full Navier-Stokes equations and not to differences between the two codes. Fourth, the effects of grid resolution were investigated using the Navier-Stokes equations. The spanwise resolution over the delta wing and the normal resolution near the upper surface were increased by a factor of 2.

All of this work was done at $\alpha = 20$ deg, a condition that did not display significant reversed flow in the previous work. In order to determine the effects of using the full Navier-Stokes equations on the reversed flow region, the $\alpha = 30$-deg case was solved using FDL3D-I. This angle of attack produced a significant region of reversed flow in the previous results.

## Analysis

The vortical flow about a delta wing ($\Gamma = 75$ deg) was simulated numerically at $\alpha = 20$ deg and 30 deg, $M_\infty = 1.95$ and $4.48 \times 10^6$. The delta wing configuration had a length of 33.9 cm, a thickness of 1.9 cm, and a leading-edge bevel $\beta = 35$ deg. Figure 1 is a sketch of the delta wing with relevant parameters labeled. This configuration was chosen to duplicate a parallel experimental study that is underway at the present time.

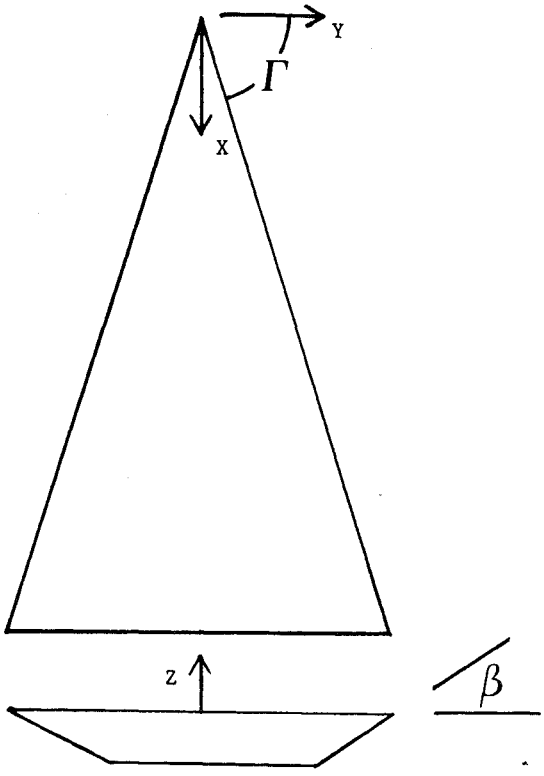


Fig. 1 Sketch of delta wing.

The governing equations were taken to be the unsteady, compressible, three-dimensional Navier-Stokes equations. The perfect gas law was used to relate the pressure, temperature and density, whereas Sutherland's equation was used to calculate the molecular viscosity. Two computer codes were used to solve this set of equations. The first, ARC3D, uses the thin-layer approximation. The second, FDL3D-I, has the option of solving either the full or thin-layer Navier-Stokes equa-

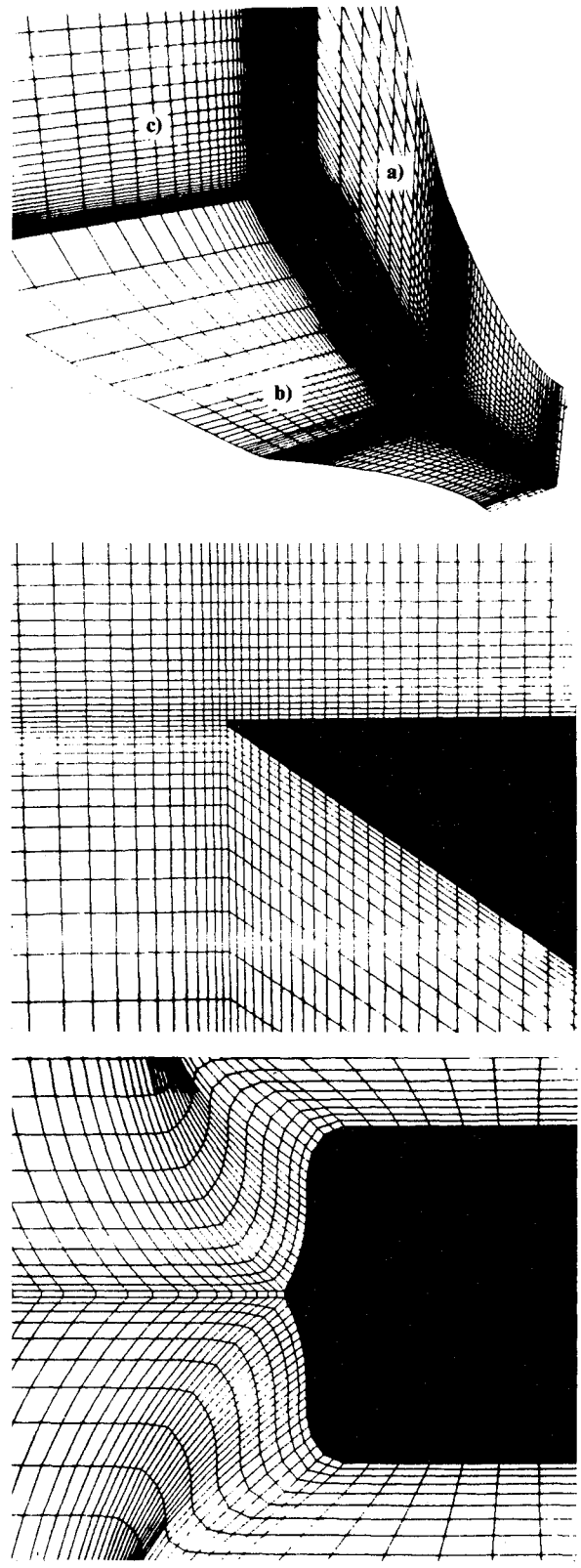


Fig. 2 Outline of the grid structure: a) global structure; b) outboard tip; c) trailing edge.

tions. The local time step for each code was scaled by $(1.0+\sqrt{J})^{-1}$, where $J$ is the Jacobian of the coordinate transformation.

The grids for these calculations were generated algebraically. The grid may be described as having an H-H structure. This type of grid was chosen to eliminate singular metrics at the leading edge and to facilitate modeling of the blunt trailing edge. Figures 2 show several planes that outline the global grid structure (Fig. 2a). The planes are the following: the symmetry plane (labeled A in the figure), the plane that contains the upper surface of the delta wing (labeled B), and the plane that is located at the downstream edge of the domain (labeled C). In addition, Figs. 2 show close-ups of the outboard tip (Fig. 2b) and the trailing edge (Fig. 2c), detailing the H-H structure. The trailing edge was rounded in order to smooth the grid. The normal grid spacing at the surface increased proportionally with the distance from the apex to a maximum of $10^{-3} \times L$ at the trailing edge. The grid was clustered in the streamwise direction at the leading and trailing edge with the spacing on the surface varying by almost three orders of magnitude. A more detailed discussion of the grid structure was reported previously.[13]

The coordinate system had its origin at the apex with the $x$ axis chordwise along the upper surface in the plane of symmetry. The $y$ axis was normal to the plane of symmetry and in the spanwise direction. The $z$ axis was normal to the upper surface and in the plane of symmetry.

The primary grid had 80 grid points in the $x$ direction with 5 ahead of the apex and 15 in the wake. In the $y$ direction, there were 49 grid points inboard of the leading edge and 31 outboard for a total of 80 grid points. In the $z$ direction, there were 80 grid points with 32 below and 48 above the delta wing. This resulted in a grid with a total of 512,000 grid points. This grid was used for the comparisons between ARC3D and FDL3D-I, the comparisons between the full and thin-layer Navier-Stokes equations using FDL3D-I, and for the turbulent calculation with ARC3D.

For the grid refinement study, a second system had an additional 49 grid points in the spanwise direction. A new grid point was inserted between each grid point on the surface. In the $z$ direction, a new point was inserted between each of the first 21 points above the upper surface. This resulted in a grid with 1,032,000 grid points.

The final grid was based on the primary mesh system with an additional 30 points in the $x$ direction. This increased the resolution at the trailing edge and matches the grid used in the previous work in which reversed flow was observed. This grid was used for the full Navier-Stokes calculation at $\alpha = 30$ deg by FDL3D-I.

Each of the simulations used the converged solution from the previous work[13] as an initial condition. The L2 norm of the change in the dependent variables displayed a spike, which then quickly decreased to its starting value. The solution was then allowed to evolve until the L2 norm reached and maintained a constant value. It should be noted that the dependent variables in ARC3D are divided by the Jacobian whereas in FDL3D-I, they are not. This results in the L2 norm differing by several orders of magnitude between the two codes. All solutions were obtained using one processor on a Cray 2 supercomputer. The data processing rate is expressed in $\mu$s/-point/iteration. The data processing rates were 39.46, 45.82, and 60.11, for ARC3D laminar, FDL3D-I thin layer, and FDL3D-I Navier-Stokes, respectively.

## Results and Discussion

The first issue dealt with was that of turbulence. ARC3D, with the turbulence model of Baldwin and Lomax, was run 1800 iterations until convergence. The L2 norm peaked at $1.2 \times 10^{-9}$ and dropped to $3.9 \times 10^{-12}$. The average value of $y^+$ on the upper surface was 4.01 with a maximum of 9.59 at the trailing edge. Figure 3 shows the pressure coefficient distribution at 81.19% root chord for the laminar and turbulent solutions (as well as data, which will be discussed later). The Reynolds number based on running length at this streamwise location was $3.63 \times 10^6$. Also shown are the data of Guyton[5] and that of Miller and Wood.[3] At this streamwise location, the average value of $y^+$ was 5.04, the minimum value was 1.76, and the maximum was 8.70. The laminar solution fell between the experimental results from the symmetry plane to the secondary separation point; the turbulent solution predicted pressure coefficients that were lower than the data. The largest difference between the two numerical simulations was 32.8% at the centerline. From the secondary separation point to the leading edge, both solutions predicted lower pressure coefficients than the data. Near the leading edge, the turbulent solution was 12.1% higher than the laminar solution, but the difference was less than the scatter in the experimental data. It appeared that the laminar solution compared more favorably with the data.

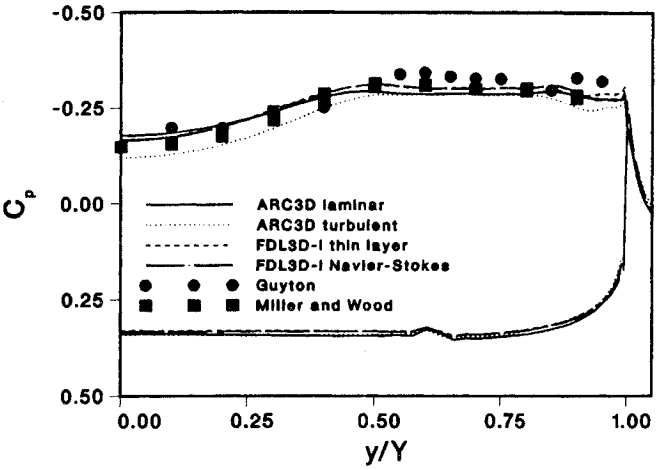


**Fig. 3 Coefficient of pressure vs $y/Y$ at 81.18% foot chord for a delta wing: $\Gamma = 75$ deg; $M_\infty = 1.95$; $\alpha = 20$ deg; $Re = 4.48 \times 10^6$.**

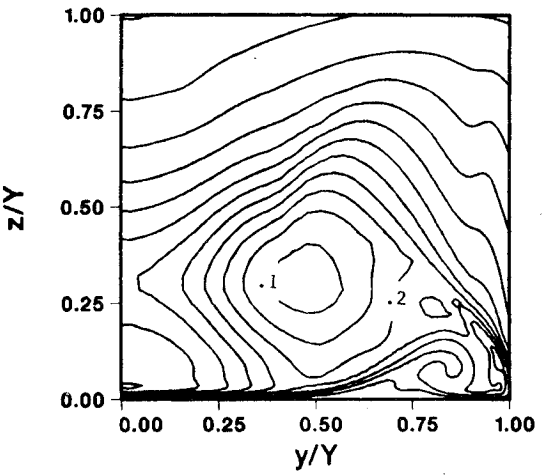


**Fig. 4 Contours of normalized pitot pressure at 81.10% root chord for a delta wing using ARC3D with no turbulence model. $\Gamma = 75$ deg; $M_\infty = 1.95$; $\alpha = 20$ deg, $Re = 4.48 \times 10^6$.**

Contours of the pitot pressure ratio at 81.19% root chord are given in Fig. 4 for the laminar solution and in Fig. 5 for the turbulent solution The modeled turbulence has no effect on the predicted location of either the primary or secondary vortex. The effect of turbulence was only apparent near the wall below the primary vortex where the boundary layer was thinner in the turbulent case.

The simulated oil flow patterns for the laminar and turbulent solutions are presented in Fig. 6. The primary, secondary, and tertiary separation and reattachment lines are all evident. They are, from the leading edge inward, the primary separa-

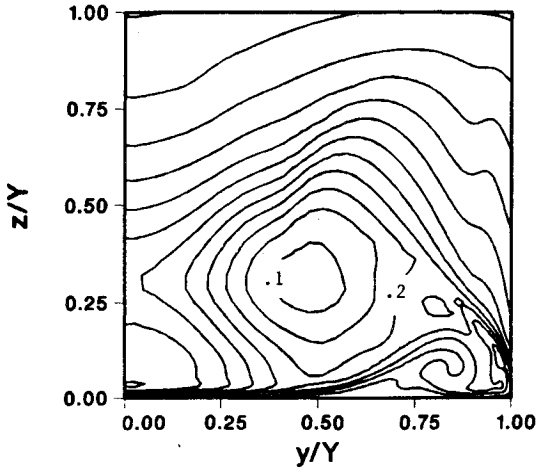


Fig. 5 Contours of normalized pitot pressure at 81.18% root chord for a delta wing using ARC3D with the Baldwin-Lomax turbulence model: $\Gamma = 75$ deg; $M_\infty = 1.95$; $\alpha = 20$ deg; $Re = 4.48 \times 10^6$.

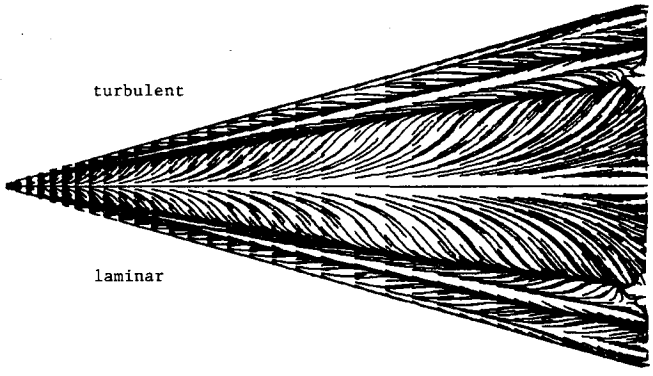


Fig. 6 Simulated oil traces for a delta wing using ARC3D turbulent (upper) and laminar (lower): $\Gamma = 75$ deg; $M_\infty = 1.95$; $\alpha = 20$ deg, $Re = 4.48 \times 10^6$.

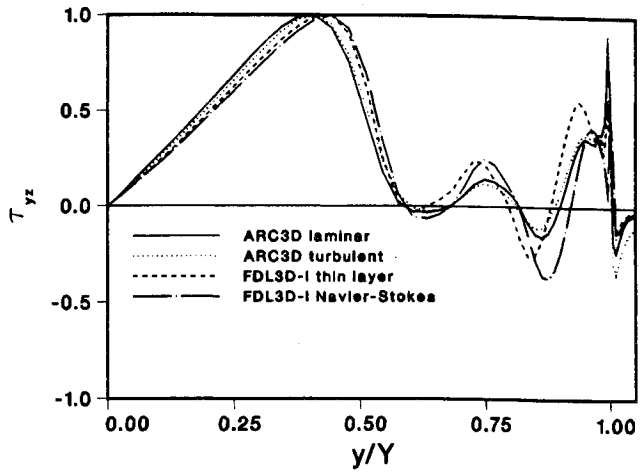


Fig. 7 Shear stress $\tau_{yz}$ vs $y/Y$ at 81.19% root chord for a delta wing: $\Gamma = 75$ deg, $M_\infty = 1.95$, $\alpha = 20$ deg, $Re = 4.48 \times 10^6$.

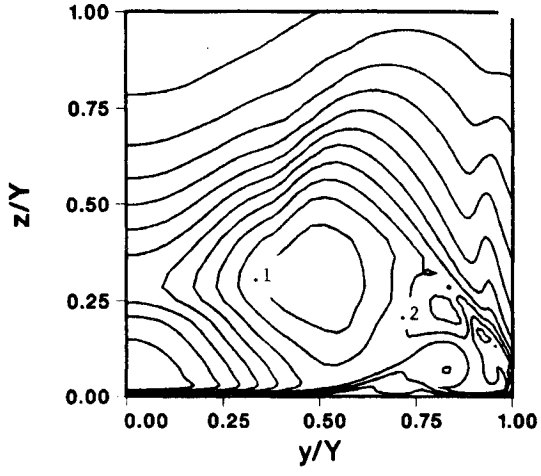


Fig. 8 Contours of normalized pitot pressure at 81.19% root chord for a delta wing using FDL3D-I thin layer: $\Gamma = 75$ deg, $M_\infty = 1.95$; $\alpha = 20$ deg; $Re = 4.48 \times 10^6$.

tion, secondary reattachment, tertiary separation, tertiary reattachment, secondary separation, and the primary reattachment at the centerline. The difference between the laminar and turbulent shear stress patterns was very minor for the entire surface. This indicated no major structural differences between the two simulations. The small changes in the separation and reattachment lines were apparent in the spanwise variation of the shear stress. Figure 7 depicts one component of the normalized surface shear stress $\tau_{yz}$ as a function of the normalized span, at 81.19% root chord. The shear stresses were normalized to their maximum at that streamwise location. The location of the reattachment and separation lines corresponds to the change of sign in $\tau_{yz}$. The secondary separation was slightly farther outboard (60.27 vs 58.82% span) for the turbulent case, whereas the secondary reattachment was inboard (89.83 vs 88.84% span).

Slight differences in pressure coefficient, pitot pressure, and shear stress distribution between the laminar and turbulent solutions were observed. The Baldwin-Lomax turbulence model is well known to be inaccurate in regions of separated flow. For $\alpha = 20$ deg, where no separations were seen, the effects of turbulence were small. At $\alpha = 30$ deg, large regions of separated flow have been previously observed, making use of the Baldwin-Lomax inappropriate. Since we are primarily interested in the assessment of the numerical procedure, accuracy, and flowfield structure, only laminar solutions were used in the remainder of this paper.

The second calculation used FDL3D-I with the thin-layer approximation. The solution required 2400 iterations using the same time step and damping coefficients that were used in the ARC3D calculation. The L2 norm peaked at $1.3 \times 10^{-3}$ and dropped to $7.6 \times 10^{-5}$. The pressure coefficient distribution at 81.19% root chord is compared to the ARC3D thin-layer result in Fig. 3. The greatest difference between them was 6.84% (at the centerline) and, in general, both were in excellent agreement with the experimental data.

Figure 8 shows contours of the pitot pressure ratio from FDL3D-I thin layer at 81.19% root chord. When compared to the ARC3D result in Fig. 4, it was seen that both codes capture the primary and secondary vortices. The predicted location of the primary vortex was almost exactly the same for the two codes. However, the secondary was farther outboard for ARC3D (81.97 vs 84.70% span). FDL3D-I was in better agreement with the experimental results from Monnerie and Werle[1] which placed the secondary at 82.5% span.

The simulated oil flow patterns compared very well over the surface and are not presented here. Both display the primary, secondary, and tertiary separation and reattachment lines. In addition, both capture a very small region of reversed flow at the trailing edge, which was observed in the previous work. The differences between the two thin-layer solutions were more apparent in the spanwise variation of the shear stress, as seen in Fig. 7. The location of the secondary separation was nearly the same for both solutions; however, the secondary reattachment, the tertiary separation, and reattachment for FDL3D-I were inboard of their locations, as predicted by ARC3D (88.02 vs 89.84% span, 79.62 vs 81.81% span, and

63.38 vs 67.69% span, respectively). The preceding results indicate that FDL3D-I (using the thin-layer equations) and ARC3D produce very similar solutions.

The third calculation used the full Navier-Stokes equations and evolved 3000 iterations with the same time step and damping terms that were used in the FDL3D-I thin-layer calculation. The L2 norm peaked at $1.15\times10^{-3}$ and dropped to $9.7\times10^{-5}$. The pressure coefficient distribution at 81.19% root chord from the full and thin layer Navier-Stokes equations are compared in Fig. 3. The two results were nearly identical for the first 80% of the span and display a 8.86% difference in the pressure coefficient near the outboard edge. There was excellent agreement with the data of Miller and Wood.[3]

Figure 9 shows contours of the pitot pressure ratio at 81.19% root chord for the FDL3D-I Navier-Stokes simulation. Comparison to the thin-layer result in Fig. 8 shows that the location of the primary vortex was nearly identical. However, the secondary vortex was farther outboard for the Navier-Stokes result (81.97 vs 85.25% span).

The simulated oil flows along the upper surface again showed only slight differences between the two solutions and are not presented here. The shear stress from the thin-layer and Navier-Stokes solutions are compared in Fig. 7. The secondary separation point for both results were nearly the same, 59.22% and 58.92% span for the thin-layer and Navier-Stokes solutions, respectively. The secondary reattachment and tertiary separation and reattachment all were further inboard for the thin-layer result (92.04 vs 88.02% span, 81.72 vs 79.62% span, and 67.87 vs 63.38% span, respectively).

From these above figures, it was concluded that differences between the thin-layer and the Navier-Stokes results were quite small for a delta wing at $\alpha=20$ deg and the thin-layer calculation (which was less expensive) captures the essential flow features.

An interpolation using the full Navier-Stokes solution was then performed to provide an initial condition for the grid resolution study. The fine grid had approximately twice as many points as the primary grid. In addition to the doubling of the computational domain, the local time step was reduced by the local scaling with the Jacobian. These two factors combined to make this an extremely expensive calculation; thus, only 600 iterations were run. This was sufficient for the L2 norm to return to its starting value. The L2 norm peaked at $7.03\times10^{-4}$ and dropped to $5.8\times10^{-5}$. Figure 10 presents the pressure coefficient distribution at 81.19% root chord. There were very slight differences between the two solutions, particularly in the region between the primary and secondary vortex. Contours of the pitot pressure ratio for the fine grid solution are presented in Fig. 11. For the region of the primary, secondary, and tertiary vortices, the fine grid solution reveals additional minute structures. These structures were also indicated in the lateral shear stress in Fig. 12. In the fine grid solution, the sep-

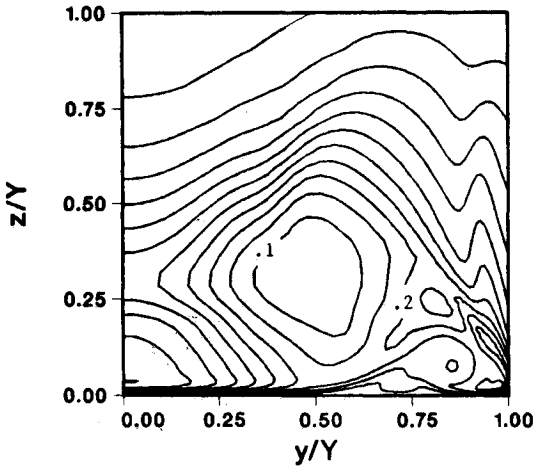


Fig. 9 Contours of normalized pitot pressure at 81.19% root chord for a delta wing using FDL3D-I Navier-Stokes: $\Gamma=75$ deg, $M_\infty=1.95$, $\alpha=20$ deg, $Re=4.48\times10^6$.

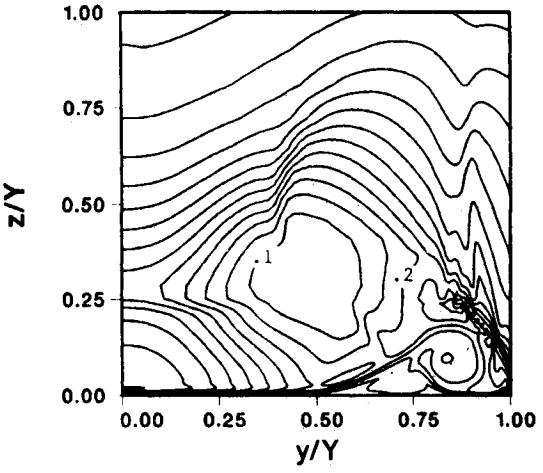


Fig. 11 Contours of normalized pitot pressure at 81.19% root chord for a delta wing using FDL3D-I with grid refinement: $\Gamma=75$ deg; $M_\infty=1.95$; $\alpha=20$ deg, $Re=4.48\times10^6$.

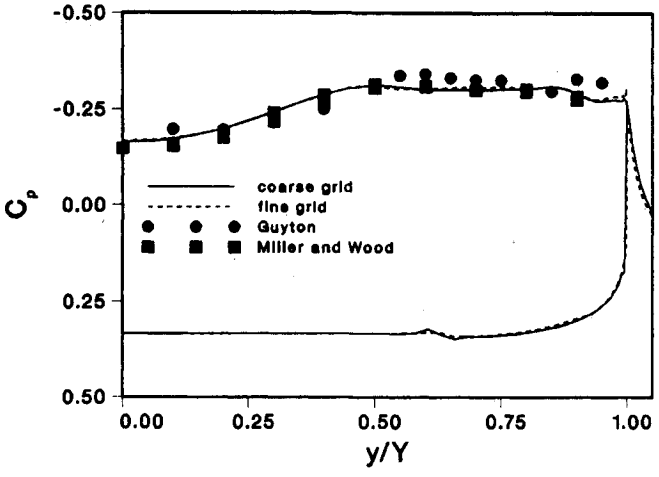


Fig. 10 Coefficient of pressure vs $y/Y$ at 81.19% root chord for a delta wing using FDL3D-I with grid refinement: $\Gamma=75$ deg, $M_\infty=1.95$; $\alpha=20$ deg, $Re=4.48\times10^6$.

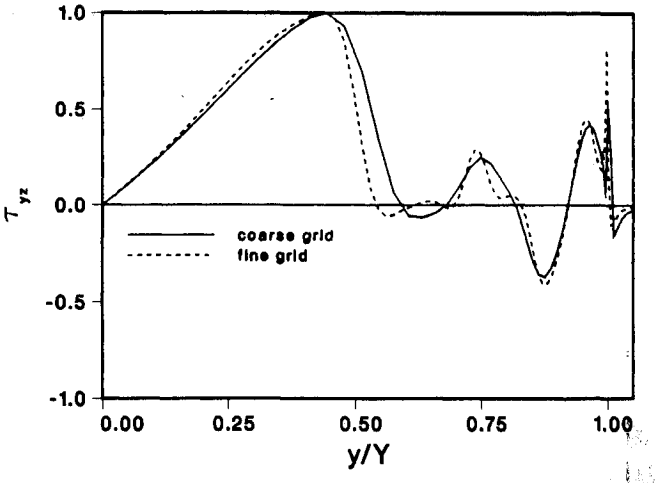


Fig. 12 Shear stress $\tau_{yz}$ vs $y/Y$ at 81.19% root chord for a delta wing using FDL3D-I with grid refinement: $\Gamma=75$ deg, $M_\infty=1.95$; $\alpha=20$ deg; $Re=4.48\times10^6$.

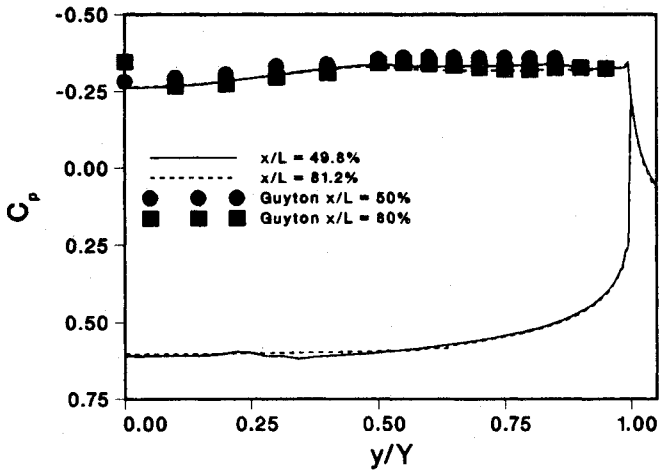


Fig. 13 Coefficient of pressure vs $y/Y$ at 49.80 and 81.19% root chord for a delta wing using FDL3D-I: $\Gamma = 75$ deg, $M_\infty = 1.95$; $\alpha = 35$ deg; $Re = 4.48 \times 10^6$.

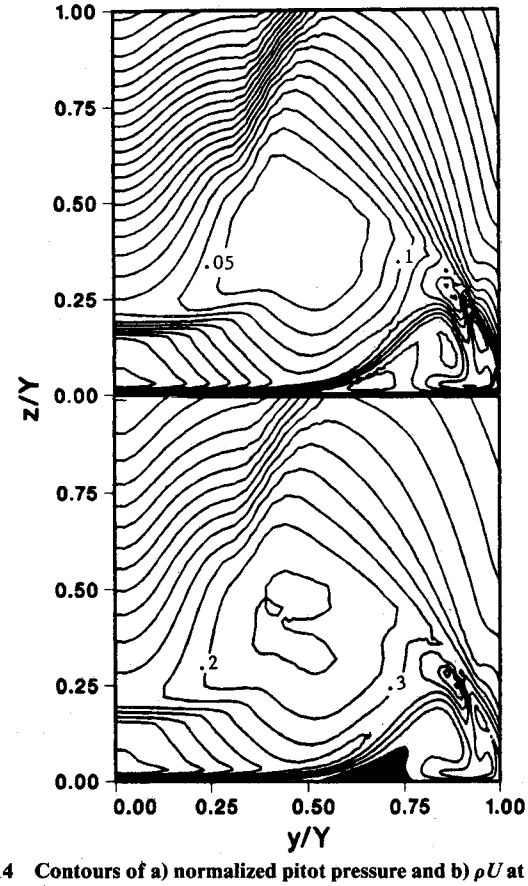


Fig. 14 Contours of a) normalized pitot pressure and b) $\rho U$ at 90.0% root chord for a delta wing, full Navier-Stokes simulation: $\Gamma = 75$ deg, $M_\infty = 1.95$; $\alpha = 35$ deg; $Re = 4.48 \times 10^6$.

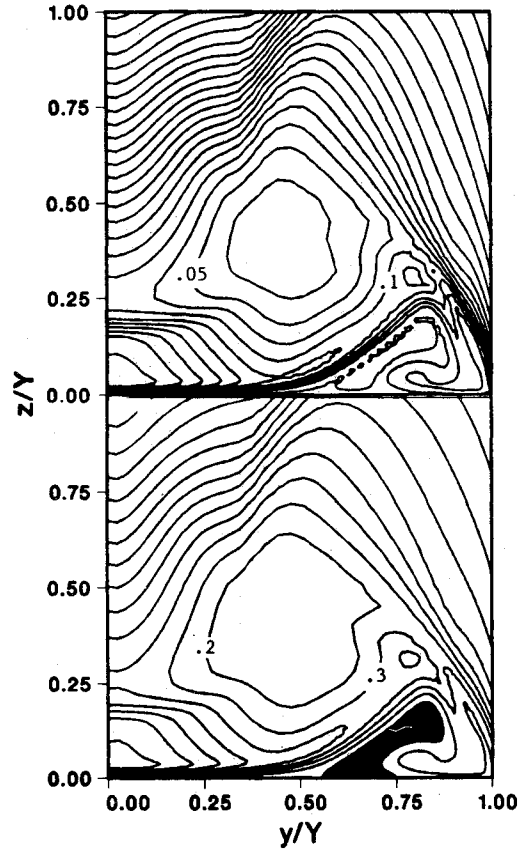


Fig. 15 Contours of a) normalized pitot pressure and b) $\rho U$ at 90.0% root chord for a delta wing, thin layer simulation from Ref. 13: $\Gamma = 75$ deg; $M_\infty = 1.95$; $\alpha = 35$ deg; $Re = 4.48 \times 10^6$.

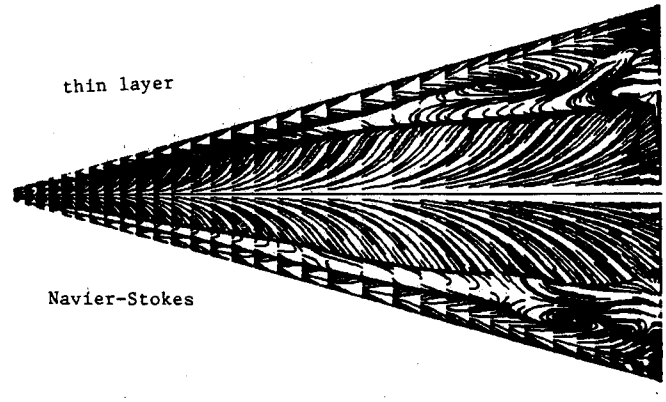


Fig. 16 Simulated oil traces for a delta wing using thin layer (upper) and Navier-Stokes (lower): $\Gamma = 75$ deg; $M_\infty = 1.95$; $\alpha = 35$ deg; $Re = 4.48 \times 10^6$.

aration between the secondary and tertiary separation points have spread laterally to accommodate the additional vortical structures.

The Navier-Stokes equations were used to calculate the flow over a delta wing at $\alpha = 30$ deg, which required 2000 iterations. The L2 norm peaked at $1.2 \times 10^{-3}$ and dropped to $8.6 \times 10^{-5}$. The pressure coefficient distribution at 49.80% and 81.19% root chord is presented in Fig. 13. Included are experimental data from Guyton[5] at 50 and 80% of the root chord. From the centerline to 45% span, the pressures were equal, but outboard they diverge with the downstream pressures being up to 5.0% higher. The agreement with the experimental data was very good. Figures 14 show contours of normalized pitot pressure (Fig. 14a) and the product of the density and the streamwise Mach number (Fig. 14b) at 89.74% root chord. This product was negative in the darkened region, indicating reversed flow. The reversed flow was contained in a region along the surface beneath the secondary vortex. Results from the previous work are presented in Figs. 15. The location of the primary vortex is the same for the two simulations. However, the height of the reversed flow region (normalized by the span) was much smaller (0.0884 compared to 0.195). This difference is due to the additional diffusion calculated in the Navier-Stokes solution.

Figure 16 depicts the surface shear map for the present Navier-Stokes solution and the previous thin-layer solution. The reversed flow region extends forward to 46% root chord

compared to 67% for the thin-layer solution. Also visible are two large counter-rotating vortical structures. In the nomenclature of Tobak and Peake[16] these are referred to as nodes. These vortices are formed by the viscous interaction between the reversed flow and the streamwise flow. The inboard vortex was swept up and inward by the primary vortex. The outboard vortex was swept up and inward by the secondary vortex. These two structures merge above the reversed flow region and are swept downstream. In the Navier-Stokes solution, the inboard and outboard nodes are located at 84.13 and 85.1% of the root chord, respectively. In the thin-layer solution, they are located at 94.23 and 76.92% of the root chord, respectively. In addition to the large nodes, a smaller node was located in each of the solutions. These nodes are too small to be discerned in Fig. 16. For the Navier-Stokes solution, the third node is located at 53.1% root chord along the secondary separation line. In the thin-layer solution, the third node is located at the trailing edge along the tertiary separation line.

These are significant differences between the thin-layer and Navier-Stokes simulations for a delta wing at $\alpha = 30$ deg. These differences manifested themselves in the secondary vortex where a shear layer is present. The variation in the streamwise and normal (to the upper surface) extent of the reversed flow region is most evident.

## Conclusions

The supersonic flowfield about a delta wing ($\Gamma = 75$ deg) was numerically simulated at $M_\infty = 1.95$ and $4.48 \times 10^6$. Two different codes based on the approximately factorized implicit Beam-Warming algorithm were used in the study. To assess the effects of turbulence, ARC3D was used with and without the Baldwin-Lomax turbulence model. The laminar and turbulent solution exhibited very little difference in the predicted vortical structure. This indicates that turbulence was not overly critical for a delta wing at $\alpha = 20$ deg with the present grid resolution.

The comparison between ARC3D and FDL3D-I (thin layer) showed minor differences in the predicted pressure coefficient distribution, location of the primary and secondary vortices, and surface shear stress. A comparison was made between the thin-layer and Navier-Stokes solutions generated by FDL3D-I. The two solutions were nearly identical, indicating that there was no advantage in using the Navier-Stokes equations over the thin layer equations of delta wing simulations at moderate angles of attack.

A calculation carried out on a refined grid for $\alpha = 20$ deg reveals that the numerical result is essentially independent from grid refinement. A calculation with FDL3D-I using the full Navier-Stokes equations was then made. For the $\alpha = 20$ deg calculation, there was no improvement with grid resolution.

Navier-Stokes solution for a delta wing at $\alpha = 30$ deg showed an embedded reverse flow region that was observed in an earlier thin-layer calculation. The dimensions of this separated flow region was significantly different from the thin-layer calculation. The reversed flow region exhibited strong velocity gradients in directions other than normal to the body surface. The thin-layer approximation does not account for the viscous term associated with these gradients.

## Acknowledgments

Computer time for the work presented here was provided under the auspices of the Air Force Weapons Laboratory at Kirtland Air Force Base. The authors wish to thank N. Rapagnani for his assistance in procuring these resources.

## References

[1]Monnerie, H., and Werle, H., "Study of Supersonic and Hypersonic Flow About a Slender Wing at an Angle of Attack," *Hypersonic Boundary Layers and Flow Fields*, AGARD CP-30, May 1968, pp. 23-1–23-19 (in French).

[2]Hummel, D., "On the Vortex Formation over a Slender Wing at Large Angles of Incidence," *High Angle of Attack Aerodynamics*, AGARD CP-247, 1987, pp. 13-1–I3-17.

[3]Miller, D. S., and Wood, R. M., "Lee-Side Flow over Delta Wings at Supersonic Speeds," NASA TP-2430, June I985.

[4]Stallings, R. L., and Lamb, M., "Wing-Alone Aerodynamic Characteristics for High Angles of Attack at Supersonic Speeds," NASA TP-I889, 1981.

[5]Guyton, R. W., private communication, 1989.

[6]Rizzetta, D. P., and Shang, J. S., "Numerical Simulation of Leading-Edge Vortex Flows," *AIAA Journal*, Vol. 24, No. 2, 1986, pp. 237–245.

[7]Buter, T. A., and Rizzetta, D. P., "Steady Supersonic Navier-Stokes Solutions of a 75° Delta Wing," NASA CP-2416, Oct., 1985.

[8]Thomas, J. L., and Newsome, R. W., "Navier-Stokes Computations of Leeside Flows Over Delta Wings," AIAA Paper 86-1949, May 1986.

[9]Scherr, S., and Das, A., "Basic Analysis of the Flow Fields of Slender Delta Wings Using the Euler Equations," International Council of the Aeronautical Sciences, Paper ICAS-88-5.2, Aug. 1988.

[10]Fujii, K., and Schiff, L. B., "Numerical Simulation of Vortical Flows Over a Strake-Delta Wing," AIAA Paper 87-1229, June 1987.

[11]Kandil, O. A., and Chung, H. A., "Unsteady Vortex Computations Past Oscillating Delta Wing at High Incidence," AIAA Paper 89-0081, June 1987.

[12]Kandil, O. A., and Chung, H. A., "Unsteady Vortex-Dominated Flows Around Maneuvering Wings Over a Wide Range of Mach Numbers," AIAA Paper 88-0317, Jan. 1988.

[13]Webster, W. P., and Shang, J. S., "Numerical Simulation of Reversed Flow Over a Supersonic Delta Wing at High Angles of Attack," AIAA Paper 89-1802, June 1989.

[14]Pulliam T. H., "Efficient Solution Methods of the Navier-Stokes Equations," *Lecture Notes for the Von Karman Institute for Fluid Dynamics Lecture Series: Numerical Techniques for Viscous Flow Computation in Turbomachinery Bladings*, Jan. 1986.

[15]Visbal M. R., "Numerical Investigation of Laminar Juncture Flows," AIAA Paper 89-1873, June 1989.

[16]Tobak, M., and Peake, D. J., "Topology of Three-Dimensional Separated Flows," *Annual Review of Fluid Mechanics*, Vol. 14, 1982, pp. 61–85.